Appl. Phys. B 54, 321–332 (1992)

Applied Physics B Photophysics and Laser Chemistry

Measurement of the Gravitational Acceleration of an Atom with a Light-Pulse Atom Interferometer

M. Kasevich and S. Chu

Physics Department, Stanford University, Stanford, CA 94305, USA

Received 26 December 1991/Accepted 10 January 1992

Abstract. Velocity sensitive stimulated Raman transitions have been used to measure the gravitational acceleration, g, of laser cooled sodium atoms in an atomic fountain geometry. By using an improved scheme to drive the Raman transitions, we have demonstrated a resolution of 3×10^{-8} g after 2×10^3 seconds of integration time. In addition to presenting recent experimental results, we review the theory of stimulated Raman transitions as it applies to atom interferometers and discuss the prospects of an atom interferometer-based gravimeter with better than 10^{-10} g absolute accuracy.

PACS: 32.80.Pj, 07.60.Ly, 35.80.+s, 42.50.Vk

Matter-wave interference with atoms has recently been demonstrated by several groups. Fringes have been observed by diffraction from two material slits in the Young's double slit geometry [1]. Interference has also been observed by diffraction from micro-fabricated gratings in a three-grating geometry [2]. The mechanical effects of light can also be used to spatially separate and interfere atomic wavepackets [3,4]. In this vein, interference effects have been demonstrated for an atomic beam interacting with four laser beams [5]. We have also demonstrated interference using laser cooled atoms and a series of three light pulses [6].

In 1975, Colella, Overhauser, and Werner demonstrated that the acceleration of a neutron due to gravity could be measured with a matter-wave interferometer [7]. Clauser subsequently noted that the inertial sensitivity of an atom interferometer could exceed that of a neutron interferometer, largely due to the atom's mass advantage and to the potential availability of sources of slow atoms [8]. Experimental demonstration of the sensitivity of atom interferometers to inertial forces came in the first generation of light-pulse atom interferometers [5, 6]. In this paper, we report on recent progress towards precise acceleration measurements using laser cooled atoms in our light-pulse atom interferometer.

Atom interferometers can be used as sensitive accelerometers in a variety of precision experiments which search for weak forces. Examples of such experiments include searches for net charge on atoms, "fifth" force experiments, and tests of general relativity. Accurate inertial sensors have practical applications in oil-well logging and navigation. Geophysical applications include earthquake prediction and studies of global warming [9].

Although the emphasis of this paper is on the experimental demonstration of high sensitivity to accelerations, the sensitivity is coupled to large ($\sim$ 6 mm) wavepacket separations. Along these lines, atom interferometers can be used for novel tests of quantum mechanics. Examples include observation of the Aharonov-Casher effect [10], "which-path" experiments [11], and Berry's phase measurements [12].

The aim of this paper is to present a unified theoretical and experimental summary of our recent work with light-pulse interferometers. In Sect. 1, we outline the general principles of operation of light-pulse interferometers. This overview is meant to motivate our approach to the problem of obtaining large wavepacket separations. Our solution relies upon the mechanical effects of stimulated Raman transitions as well as the long measurement times available with laser cooled atoms in an atomic fountain. We present a theoretical review of the aspects of stimulated Raman transitions relevant to the interferometer in Sect. 2. Section 3 draws on the results of Sect. 2 to analyze the behavior of an atomic wavepacket in the interferometer. The discussion then turns to experimental demonstration of interference. Section 4 describes the laser cooling and trapping techniques used to create the atomic fountain. The details of the interferometer experiment are presented in Sect. 5, and our recent results are given in Sect. 6. The results are discussed in the context of prospects for improved acceleration measurements in Sect. 7.

1 Light-Pulse Interferometers

Light-pulse interferometers work on the principle that when an atom absorbs or emits a photon momentum must be conserved between the atom and the light field. Consequently, an atom which emits (absorbs) a photon of momentum $\hbar\mathbf{k}$ will receive a momentum impulse of $\delta\mathbf{p} = -\hbar\mathbf{k}\,(+\hbar\mathbf{k})$. When a resonant travelling wave is used to excite an atom, the internal state of the atom becomes correlated with its momentum: an atom in its ground state $|1\rangle$ with momentum $\mathbf{p}$ (labelled $|1,\mathbf{p}\rangle$) is coupled to an excited state $|2\rangle$ of momentum $\mathbf{p}+\hbar\mathbf{k}$ ($|2,\mathbf{p}+\hbar\mathbf{k}\rangle$) [3].

We use a $\pi/2$–π–$\pi/2$ pulse [13] sequence to coherently divide, deflect and finally recombine an atomic wavepacket (see Fig. 1). The first $\pi/2$ pulse excites an atom initially in the $|1,\mathbf{p}\rangle$ state into a coherent superposition of states $|1,\mathbf{p}\rangle$ and $|2,\mathbf{p}+\hbar\mathbf{k}\rangle$. If state $|2\rangle$ is stable against spontaneous decay, the two wavepackets will drift apart by a distance $\hbar\mathbf{k}T/m$ in time T. Each wavepacket is redirected by a π pulse which induces the transitions $|1,\mathbf{p}\rangle \rightarrow |2,\mathbf{p}+\hbar\mathbf{k}\rangle$ and $|2,\mathbf{p}+\hbar\mathbf{k}\rangle \rightarrow |1,\mathbf{p}\rangle$. After another interval T the wavepackets once again overlap. A final $\pi/2$ pulse causes the two wavepackets to interfere. The interference is detected, for example, by measuring the number of atoms in the $|2\rangle$ state.

We obtain large wavepacket separations by using laser cooled atoms in an atomic fountain geometry [14] and velocity sensitive stimulated Raman transitions to drive the transition [15]. The atomic fountain geometry allows the drift times T to be on the order of a second. Stimulated Raman transitions give large recoil kicks $\hbar\mathbf{k}/m$ in transitions between ground-state hyperfine levels.

2 Stimulated Raman Transitions

Drift times as large as 0.5 s are feasible using laser cooled atoms in an atomic fountain geometry. For the light-pulse interferometer described above, this requires an atomic transition which is metastable on this time scale. Groundstate hyperfine transitions easily fulfill the requirement of metastability. Unfortunately, the single photon recoil velocities are small (0.1 μm/s for the Na $F=1, 3S_{1/2} \rightarrow F=2, 3S_{1/2}$ transition). Metastable optical transitions, on the other hand, have large recoil velocities, but ultra-stable lasers are needed to drive the transitions.

Under certain circumstances, a two-photon Raman transition can satisfy the metastability criterion as well as provide large recoil velocities. Consider an atom illuminated by two counter-propagating light beams whose frequency difference is nearly equal to a ground-state hyperfine transition (see Fig. 2). Each light beam is nearly resonant with an allowed optical transition, but far enough detuned from that transition so that the spontaneous emission rate from that level is negligible. Under these circumstances, the three level system reduces to a two level system coupled by a two-photon Raman transition [16].

Because the beams are counter-propagating, the recoil momentum associated with the transition is the *sum* of the momentum of each optical photon. For the sodium $3S_{1/2} \rightarrow 3P_{3/2}$ transitions, the two-photon recoil velocity is ~6 cm/s. The transition probability, however, depends on the *difference* of the frequencies of the two light beams. The difference frequency can be set, for example, by a phase-modulator driven by a stable rf oscillator [15] or by phase locking the beat note between two laser beams to a stable rf source [17]. In either case, the optical frequencies are correlated, so that any frequency jitter in the laser source does not effect the Raman difference frequency and hence the dynamics of the atom–laser interaction.

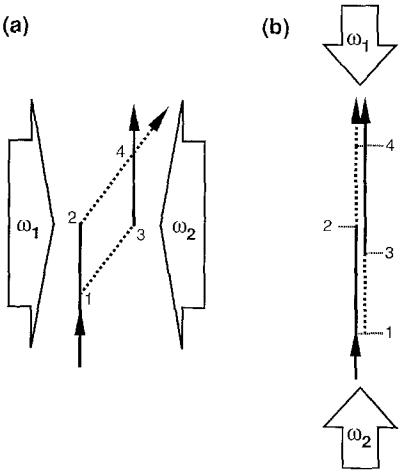

Fig. 1a, b. Paths of an atom in the interferometer. Lines represent the mean position of the wavepacket as a function of time. Solid lines correspond to atom's in internal state $|1\rangle$; dashed lines to atoms in state $|2\rangle$. The velocity recoil from the first $\pi/2$ pulse will divides the atom at position 1. A π pulse redirects the atom at positions 2 and 3. A final $\pi/2$ pulse interferes the wavepackets at position 4. The relative phases of the interfering wavepackets determine state of the atom after the final pulse. **a** Mach-Zehnder configuration: atom's velocity perpendicular to laser beams. **b** Gravimeter configuration: atom's velocity parallel to laser beams

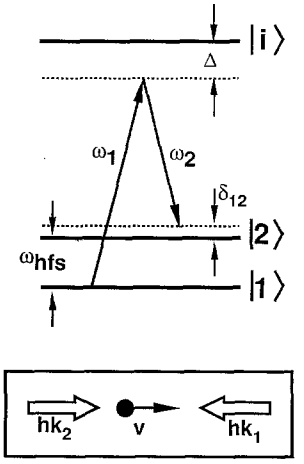

Fig. 2. Energy diagram for Raman transitions. The inset shows the geometry for the velocity sensitive configuration. The Raman transitions are between groundstate hyperfine levels $|1\rangle$ and $|2\rangle$. Laser beams are detuned by a frequency Δ from the optical transition $|i\rangle$. Population is resonantly transferred from $|1\rangle$ to $|2\rangle$ when the frequency difference $\omega_1-\omega_2$ is nearly equal to ω_{hfs}. The detuning δ_{12} depends on the velocity of the atom along the laser beams. In making the transition $|1\rangle \rightarrow |2\rangle$, the atom's momentum changes by $\hbar\mathbf{k}_1 - \hbar\mathbf{k}_2$

2.1 Theory of Stimulated Raman Transitions [18]

The Hamiltonian for the three level system is

$$\hat{H} = \frac{\hat{p}^2}{2m} + \hbar\omega_1^{\mathrm{A}}|1\rangle\langle 1| + \hbar\omega_2^{\mathrm{A}}|2\rangle\langle 2| + \hbar\omega_i^{\mathrm{A}}|i\rangle\langle i| + \hat{V}\,, \quad (1)$$

where $\hat{V}$ describes the atom–field interaction, and $\hbar\omega_\alpha^{\mathrm{A}}$ is the internal energy of state $|\alpha\rangle$. In the electric dipole approximation, the coupling of the atom to the Raman light field is

$$\begin{aligned}\hat{V} &= -e\mathbf{r}\cdot\mathbf{E}\\ \mathbf{E} &= +\mathbf{E}_1\cos(k_1x - \omega_1 t + \Phi_1)\\ &\quad + \mathbf{E}_2\cos(k_2x - \omega_2 t + \Phi_2)\,.\end{aligned} \quad (2)$$

The frequencies $\omega_1, \omega_2 \sim \omega_i^{\mathrm{A}} - \omega_1^{\mathrm{A}}$ while the difference $\omega_1 - \omega_2 \sim \omega_{\mathrm{hfs}} = \omega_2^{\mathrm{A}} - \omega_1^{\mathrm{A}}$ (see Fig. 2). For counterpropagating beams $k_1 \approx -k_2$. We have explicitly neglected spontaneous emission in the off-resonant excitation of the optical transition.

Using free-space momentum eigenstates to characterize the center-of-mass motion of the atom, we look for solutions to the Schrödinger equation of the form

$$|\psi\rangle = \int dp \sum_\alpha a_{\alpha,p}(t)\,\mathrm{e}^{-\mathrm{i}\left(\omega_\alpha^{\mathrm{A}} + \frac{p^2}{2m}\right)t}|\alpha, p\rangle\,, \quad (3)$$

where $|\alpha, p\rangle$ corresponds to an atom in internal state $|\alpha\rangle$ and in momentum eigenstate $\psi_p(x) \sim \mathrm{e}^{\mathrm{i}px/\hbar}$. For a given momentum, the Schrödinger equation reduces to

$$\begin{aligned}\dot{a}_{1,p} &= \frac{\mathrm{i}}{2}\mathrm{e}^{\mathrm{i}\Delta_1 t}\Omega_{1i}^* a_{i,p+\hbar k_1}\,,\\ \dot{a}_{i,p+\hbar k_1} &= \frac{\mathrm{i}}{2}[\Omega_{i1}\mathrm{e}^{-\mathrm{i}\Delta_1 t}a_{1,p}\\ &\quad + \Omega_{i2}\mathrm{e}^{-\mathrm{i}\Delta_2 t}a_{2,p+\hbar k_1-\hbar k_2}]\,,\\ \dot{a}_{2,p+\hbar k_1-\hbar k_2} &= \frac{\mathrm{i}}{2}\mathrm{e}^{\mathrm{i}\Delta_2 t}\Omega_{1i}^* a_{i,p+\hbar k_1}\,,\end{aligned} \quad (4)$$

where

$$\begin{aligned}\Omega_{ji} &= \frac{e}{\hbar}\langle i|\mathbf{r}\cdot\mathbf{E}_j|j\rangle\mathrm{e}^{\mathrm{i}\Phi_j}\,,\\ \Delta_j &= (\omega_j^{\mathrm{A}} + \omega_j - \omega_i^{\mathrm{A}}) + \frac{p_j^2}{2m} - \frac{p_i^2}{2m}\,.\end{aligned} \quad (5)$$

In the above equations, the index $j = 1, 2$, while the index i refers to the intermediate state. The momentum associated with state $|1\rangle$ is $p_1 = p$, with state $|2\rangle$ is $p_2 = p + \hbar k_1 - \hbar k_2$, and with state $|i\rangle$ is $p_i = p + \hbar k_1$. For simplicity we have assumed that the electric fields $\mathbf{E}_j$ couple only to the $|j\rangle \to |i\rangle$ transitions. This is a good approximation when ω_{hfs} is larger than the detuning Δ from the optical resonance. The rotating wave approximation has been used to obtain the above coupled equations.

Adiabatic elimination of level $|i\rangle$ results in the familiar equations for a two-level atom in an external driving field:

$$\begin{aligned}\dot{a}_{1,p} &\approx -\frac{\mathrm{i}}{2}\Omega_1^{\mathrm{AC}}a_{1,p} - \frac{\mathrm{i}}{2}\mathrm{e}^{\mathrm{i}\delta_{12}t}\Omega_{\mathrm{eff}}a_{2,p+\hbar k_1-\hbar k_2}\,,\\ \dot{a}_{2,p+\hbar k_1-\hbar k_2} &\approx -\frac{\mathrm{i}}{2}\Omega_2^{\mathrm{AC}}a_{2,p+\hbar k_1-\hbar k_2} - \frac{\mathrm{i}}{2}\mathrm{e}^{-\mathrm{i}\delta_{12}t}\Omega_{\mathrm{eff}}^* a_{1,p}\,,\end{aligned} \quad (6)$$

where

$$\begin{aligned}\Omega_{\mathrm{eff}} &= \frac{\Omega_{1i}^*\Omega_{i2}}{2\Delta}\,,\\ \Omega_j^{\mathrm{AC}} &= \frac{|\Omega_{ji}|^2}{2\Delta}\,,\\ \delta_{12} &= (\omega_1 - \omega_2)\\ &\quad - \left[\omega_{\mathrm{hfs}} + v_x(k_1 - k_2) + \hbar\frac{(k_1 - k_2)^2}{2m}\right].\end{aligned} \quad (7)$$

Here v_x is the projection of the atom's velocity along the laser beams. Since the equations reduce to those of a two-level system, the NMR language used to describe the interferometer in Sect. 1 applies equally well to those which employ two-photon Raman transitions. Momentum recoil explicitly shows up in the coefficients of (6), where there is a one-to-one correlation between the atom's internal state and its momentum. The first terms on the right of (6) lead to ac Stark shifts of levels $|1\rangle$ and $|2\rangle$. The second terms lead to Rabi flopping between the two levels. Note that the effective Rabi frequency Ω_{eff} depends on the initial phase of the light fields. This dependence eventually leads to the atom's sensitivity to inertial forces during a $\pi/2$–π–$\pi/2$ pulse sequence.

The effective detuning δ_{12} from the Raman resonance contains three terms: ac Stark shifts, Doppler shifts, and the recoil shift. The ac Stark shifts arise from the weak coupling of levels $|1\rangle$ and $|2\rangle$ to level $|i\rangle$. They are typically on the order of the effective Rabi frequency Ω_{eff}. The Doppler shifts arise from the atom's motion along the laser beams. In the atom's frame of reference, the frequency of each light beam is Doppler shifted by an amount $k_i v_x$. The Raman resonance, therefore, shifts by $(k_1 - k_2)v_x \sim 2kv_x$ when the beams are counter-propagating and of nearly the same frequency. For sodium, where the lasers are resonant with the $3P_{3/2}$ transition, this amounts to 33 kHz for an atom with a velocity of 1 cm/sec along the beams. The Doppler sensitivity of these transitions has been the subject of a previous study, where we have used the transitions to select ensembles of atoms with extremely narrow velocity spreads [15].

Although the levels $|1\rangle$ and $|2\rangle$ have been described as groundstate hyperfine levels, the above considerations apply equally well to transitions between magnetic sublevels within a given hyperfine level (e.g., $F, m_f = -1 \to F$, $m_f = +1$) [19]. These transitions, however, are unsuitable for interferometers configured as inertial sensors as they are first order sensitive to magnetic field variations (see below).

The hyperfine structure of the intermediate level, although not explicitly considered above, needs to be incorporated into the theory in order to calculate effective Rabi frequencies for real atoms. The hyperfine structure of level $|i\rangle$ is included by replacing the single state $|i\rangle$ with a multiplet of levels. Again, by adiabatically eliminating these levels, equations of the form of (4) reduce to the form of (6). The effective Rabi frequency is now given by a sum over intermediate levels

$$\Omega_{\mathrm{eff}} = \sum_i \frac{\Omega_{1i}^*\Omega_{i2}}{2\Delta_i}\,, \quad (8)$$

where the index i ranges over all intermediate states.

2.2 Raman Transitions Using Phase-Modulated Lasers

It was assumed above that only two frequency components were present in the driving light field. In our experiment, an electro-optic phase-modulator generated the frequency offset for the Raman transitions. Thus, in practice, the light field contained several frequency components. This situation is readily incorporated into the above theoretical framework by explicitly including these fields in the coupling potential $\hat{V}$.

In our earlier experiments one of the two counter-propagating beams passed through a phase-modulator and the other through an acousto-optic frequency shifter. The Raman frequency was determined by the difference frequency between one of the frequency sidebands of the phase-modulated beam and the frequency shifted counter-propagating beam. The other, non-Raman resonant, frequency components effect the atom only by contributing additional ac Stark shift terms to the resonance condition.

In the present experiment, the Raman transition is driven by phase-modulating both Raman beams. The second, counter-propagating beam, is generated by simply retroreflecting the first beam on a stationary mirror. The Raman frequency is now determined by the modulation frequency alone. Analysis of this geometry is complicated by the interference between several pairs of Raman resonant sidebands, as well as potentially troublesome contributions from Doppler insensitive Raman processes and from standing wave diffraction.

Since the frequencies ω_1 and ω_2 come from both directions, there are two Doppler sensitive resonances, one at $+v_{\text{res}}$ and the other at $-v_{\text{res}}$, where v_{res} is the velocity along the beam for which an atom is resonant with the Raman field. In order to maintain a unique correlation between internal state and momentum, the Doppler shift $2\,\text{k}v_{\text{res}}$ must be greater than the Rabi frequency, so that only one spatial combination of ω_1 and ω_2 drives the atom. In this limit, Doppler insensitive Raman processes and standing wave diffraction from same frequency beams also become unimportant. Standing wave diffraction results from two-photon transitions which involve counter-propagating beams of the same frequency and polarization. Doppler insensitive Raman terms are out of resonance when the sideband frequency is tuned to one of the Doppler sensitive resonances. In the experiment, the Doppler shifts $2\,\text{k}v_{\text{res}}$ were always at least 10 times the effective Rabi frequency.

In the weak phase-modulation limit the Raman field has three significant frequency components: a carrier and two sidebands. Thus the total electric field consists of three standing waves of frequency $\omega-\omega_{\text{rf}}$, ω, and $\omega+\omega_{\text{rf}}$ respectively. The Raman transition is now driven by two possible frequency combinations ω and $\omega-\omega_{\text{rf}}$, and ω and $\omega+\omega_{\text{rf}}$, and the two Raman amplitudes will interfere. Using this electric field in (2) we again reduce (4) to the form of (6). In doing so we have assumed the processes described in the previous paragraph to be Doppler shifted out of resonance. With the approximation that the atomic wavepacket is well localized on the scale length $k_{\text{rf}}=\omega_{\text{rf}}/c$, the effective Rabi frequency is given by

$$\Omega_{\text{eff}}(l)=\frac{\Omega_+^*\Omega_{\text{c}}}{2\Delta_+}\text{e}^{\text{i}k_{\text{rf}}l}+\frac{\Omega_{\text{c}}^*\Omega_-}{2\Delta_{\text{c}}}\text{e}^{-\text{i}k_{\text{rf}}l}\,, \tag{9}$$

where l is the distance of the wavepacket from the retroreflecting mirror; Ω_-, Ω_{c}, and Ω_+ are the one photon Rabi frequencies for the lower sideband, carrier, and upper sideband, respectively; and Δ_+ and Δ_{c} the detuning from the $|1\rangle\rightarrow|i\rangle$ optical transition for the upper sideband and carrier. Note that Ω_{eff} has a slowly varying spatial dependence on the scale length of k_{rf} (λ_{rf} for sodium is $\sim$18 cm).

3 Interferometer Theory

In the absence of any external forces acting on the atom, the solutions to (6) and those for the free evolution of the wavepacket can be used to obtain the final state of the atom after the $\pi/2$–π–$\pi/2$ interferometer pulse sequence. We show below that the final state of the atom depends on the phase of the Raman light field driving the transition. This result is readily extended to an atom falling in a gravitational field. In the reference frame falling with the atom, the Raman light field's frequencies appear to be Doppler shifted linearly with time. This frequency chirp shows up as a quadratic shift in the *phase* of the field as a function of time.

In Sect. 2 we analyzed the atom's center of mass motion in terms of momentum eigenstates. In Sect. 3.1 we analyze interferometer phase shifts in terms of momentum eigenstates. This has the advantage that the calculations are straight forward but the disadvantage that the range of applicability of the solutions is limited. For example, it is awkward to handle external electric or magnetic field gradients in this basis set. The phase shifts can also be viewed in terms of the wavepacket's mean position. Since accounts of this analysis have been presented elsewhere, we simply quote the results for comparison in Sect. 3.2. In Sect. 3.3 we discuss the issue of fringe visibility in the context our interferometer.

3.1 Phase Shifts for Momentum Eigenstates

In the limit of short, intense driving fields ($\Omega_{\text{eff}}\gg\delta_{12}$) (6) can be solved for the amplitudes $a_{1,p}$ and $a_{2,p+2\hbar k}$ (taking $k_1\approx-k_2$) immediately following a $\pi/2$ or π pulse. For a $\pi/2$ pulse of duration $\tau/2$, or a π pulse of duration τ, the amplitudes are [20]

$$\begin{aligned}
a_{1,p}(t+\tau/2)&=\sqrt{\tfrac{1}{2}}[a_{1,p}(t)-\text{i}\text{e}^{+\text{i}\phi(t)}a_{2,p+2\hbar k}(t)]\,,\\
a_{2,p+2\hbar k}(t+\tau/2)&=\sqrt{\tfrac{1}{2}}[-\text{i}\text{e}^{-\text{i}\phi(t)}a_{1,p}(t)\\
&\qquad+a_{2,p+2\hbar k}(t)]\,,\\
a_{1,p}(t+\tau)&=-\text{i}\text{e}^{+\text{i}\phi(t)}a_{2,p+2\hbar k}(t)\,,\\
a_{2,p+2\hbar k}(t+\tau)&=-\text{i}\text{e}^{-\text{i}\phi(t)}a_{1,p}\,,
\end{aligned} \tag{10}$$

where

$$\phi(t)=\int_{t_0}^{t}\delta_{12}(t')\,dt'\,. \tag{11}$$

During the period between pulses, the free evolution is

$$\begin{aligned} a_{1,p}(t+T) &= a_{1,p}(t)\,, \\ a_{2,p+2\hbar k}(t+T) &= a_{2,p+2\hbar k}(t)\,. \end{aligned} \tag{12}$$

[Note that the explicit time dependence of the amplitudes has been factored out in the definition of $a_{\alpha,p}(t)$ in (3)]. Evaluating (10) and (12) for the three pulse interferometer sequence leads to the following expression for the transition probability to state $|2\rangle$ for an atom initially prepared in state $|1\rangle$:

$$a_{2,p+2\hbar k}(2T+2\tau) = \tfrac{1}{2}(e^{-i\Delta\phi}+1)\,, \tag{13}$$

where

$$\Delta\phi = \phi(t_1) - 2\phi(t_2) + \phi(t_3)\,, \tag{14}$$

and t_1 is the time of the first $\pi/2$ pulse of width $\tau/2$, $t_2 = \tau/2 + T + t_1$ is the time of the π pulse, and $t_3 = 3\tau/2 + 2T + t_1$ the time of the final $\pi/2$ pulse.

$\Delta\phi$ does not vary with the initial momentum of the atom. This has the important consequence that a large spread in initial velocities can coherently contribute to the interference signal. Equation 14 was derived for one momentum component of a wavepacket. Since it is independent of momentum, the phase shift for a spatially localized wavepacket, which is a coherent sum over momentum states, is also given by this equation. Specifically, for ω_1, ω_2 independent of time, $\Delta\phi = 0$. AC Stark shifts lead to no net shift $\Delta\phi$ if the intensity of the Raman field remains constant for all three pulses. Consequently, phase shifts associated with the AC Stark terms have been suppressed in (10).

Next consider an atom which is falling in a gravitational field. In the frame falling with the atom the Raman frequency changes linearly with time at the rate of $(\mathbf{k}_1 - \mathbf{k}_2)\cdot\mathbf{g}t$. Evaluating (14) with $\omega_1 - \omega_2 \to \omega_1 - \omega_2 - (\mathbf{k}_1 - \mathbf{k}_2)\cdot\mathbf{g}t$ gives

$$\Delta\phi = -(\mathbf{k}_1 - \mathbf{k}_2)\cdot\mathbf{g}T^2\,. \tag{15}$$

For sodium, with $\mathbf{k}_1, \mathbf{k}_2$ parallel to $\mathbf{g}$, $(k_1 - k_2)g \sim 2\pi \times 3.3 \times 10^7\ \mathrm{s}^{-2}$.

In the experiment the effective Rabi frequency was $\sim 50\,\mathrm{kHz}$, whereas the change in the Doppler shifts, $\sim 2k_1gT$, was greater than 3 MHz. Thus a momentum component in resonance with the first $\pi/2$ pulse will be far out of resonance with the remaining pulses. By actively changing the frequency difference $\Delta\omega(t) = \omega_1(t) - \omega_2(t)$, we compensated for the atom's deceleration. We changed $\omega_1(t) - \omega_2(t)$ so that, for each Raman pulse, the detuning from resonance was less than the Rabi frequency. The atom is resonantly driven for all three pulses when $\Delta\omega = \omega_0$ for the first $\pi/2$ pulse, $\Delta\omega = \omega_0 + \omega_m$ for the π pulse, and $\Delta\omega = \omega_0 + 2\omega_m$ for the final $\pi/2$ pulse, with $\omega_m \sim (\mathbf{k}_1 - \mathbf{k}_2)\cdot\mathbf{g}T$. In the falling frame, the phase of the Raman field before each Raman pulse is $\omega_0 t_1 + \phi_1^0$, $(\omega_0+\omega_m)t_2 - (\mathbf{k}_1 - \mathbf{k}_2)\cdot\mathbf{g}t_2^2 + \phi_2^0$, and $(\omega_0 + 2\omega_m)t_3 - (\mathbf{k}_1 - \mathbf{k}_2)\cdot\mathbf{g}t_3^2 + \phi_3^0$ respectively. In this case, $\Delta\phi = 2\omega_m T - (\mathbf{k}_1 - \mathbf{k}_2)\cdot\mathbf{g}T^2 + \Delta\phi^0$. The term $\Delta\phi^0 = \phi_1^0 - 2\phi_2^0 + \phi_3^0$ represents the initial phase relationship between the three pulse frequencies. If each of the three frequencies is derived from an independent synthesizer, the ϕ_i^0's are interpreted as the phase of the i^{th} synthesizer at time $t = 0$. [e.g., $\phi_i(t) = \Delta\omega_i t + \phi_i^0$)].

Rather than using three independent frequencies, the resonance could equally well have been maintained by a phase continuous sweep of the frequency difference $\Delta\omega$, so that $\Delta\omega(t) = \omega_0 + \beta(t - t_0)$. Evaluation of (14) in the falling frame, for this condition gives $\Delta\phi = [\beta - (\mathbf{k}_1 - \mathbf{k}_2)\cdot\mathbf{g}]T^2$. When $\beta = (\mathbf{k}_1 - \mathbf{k}_2)\cdot\mathbf{g}$ there is no relative phase shift: the Doppler shift is exactly canceled by the frequency sweep of the Raman driving field. Note that this expression is insensitive to the time origin of the sweep (t_0). The accuracy of the phase continuous sweep is critical if the full resolution for the interferometer is to be realized. The introduction of direct frequency synthesis techniques allows phase continuous sweeps while remaining locked to a stable frequency reference oscillator.

3.2 Phase Shifts for Wavepackets

The method of Sect. 3.1 shows the origin of gravitationally induced phase shifts to be Doppler shifts of the Raman field. However, it does not provide a useful framework for understanding phase shifts due to non-inertial forces. An alternative approach, which can account for non-inertial forces, views phase shifts in terms of the position of the wavepacket [5, 6]. Here we will only summarize the results. In this approach, contributions to $\Delta\phi$ fall into two classes: those arising from the atom's interaction with the light ($\Delta\phi_l$) and those arising during the atom's free evolution between light pulses ($\Delta\phi_f$). The first take the form

$$\begin{aligned} \Delta\phi_l = {} & \phi_R(x_1^1, t_1) - \phi_R(x_2^1, t_2) \\ & - \phi_R(x_2^2, t_2) + \phi_R(x_3^1, t_3), \end{aligned} \tag{16}$$

where $\phi_R(\mathbf{x}, t) = (\mathbf{k}_1 - \mathbf{k}_2)\cdot\mathbf{x} - \Delta\omega t$ is the phase of the Raman field at position $\mathbf{x}$ and time t. The position vectors $\mathbf{x}_i^\alpha$ represent the mean position of the wavepacket correlated with internal state α at the time t_i. When the action $S = \int_\Gamma L dt$ (L the Lagrangian for the atom) is much greater than $\hbar$, the free evolution contribution is [21]

$$\Delta\phi_f = \int_\Gamma \mathbf{k}_a \cdot d\mathbf{x} - \omega_a dt\,, \tag{17}$$

where Γ is the circuit describing the path of the wavepackets, $\mathbf{k}_a$ =(wavepacket's mean momentum $\mathbf{p}$)/$\hbar$, and ω_a =(total mean energy of wavepacket)/$\hbar$.

Evaluation of (16) for the gravitationally perturbed wavepacket trajectories which occur in a $\pi/2$–π–$\pi/2$ pulse sequence yields the result obtained in Sect. 3.1. The free evolution contribution from (17) turns out to be zero if there is no violation of the equivalence principle: the contribution from the asymmetry in de Broglie wavelengths is canceled by the changes in the atom's total energy. This is in contrast to neutron interferometers of the type described in [7], where the free evolution contribution *is* the dominant phase shift [22]. The distinguishing feature between the two cases is that the energy of the particle is not conserved during the light pulses of our interferometer while it is conserved during the Bragg reflection processes of neutron interferometers.

3.3 Fringe Visibility

Fringe visibility $V = (P_{max} - P_{min})/(P_{max} + P_{min})$ quantifies the extent to which wavepacket interference is experimentally observable. For our interferometer P_{max} and P_{min} are the maximum and minimum probabilities of finding the atom in state $|2\rangle$ after the $\pi/2$–π–$\pi/2$ pulse sequence. If the conditions for the validity of (10) are satisfied, the visibility is 100%. However, the assumption that the Rabi frequency be much larger than the detuning from the transition is not true for all atoms contributing to the signal. The Doppler width of the laser cooled source of atoms is 600 kHz while the maximum Rabi frequency used was 50 kHz. Consequently, not all atoms see a $\pi/2$–π–$\pi/2$ pulse sequence because some are Doppler shifted out of resonance with the Raman beams. Contributions from off-resonant atoms are calculated by using the exact solutions to (6) rather than the approximate ones given by (10). Figures 3a, b show the probability of excitation to level $|2\rangle$ following a $\pi/2$–π–$\pi/2$ sequence as a function of the atom's detuning from the resonance. In Fig. 3b the phase of the final $\pi/2$ pulse is shifted by π radians with respect to the first two pulses. In the limit where the Doppler width of the source of atoms is much larger than the Rabi frequency, P_{max} and P_{min} are obtained by integrating the excitation probabilities over detuning (velocity). The resulting visibility is 27% in the limit where $T \gg \tau$. The approximations for the validity of (10) amount to considering only those detunings near the center of curves of Figs. 3a, b.

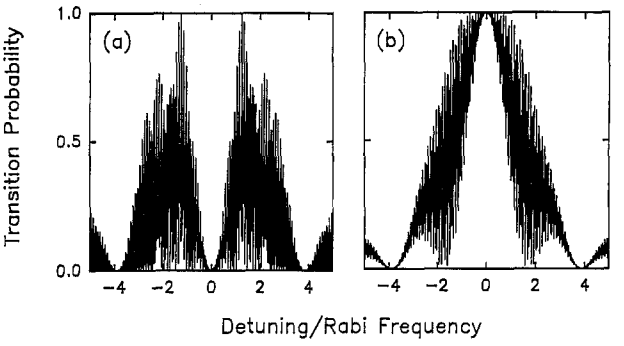

Fig. 3a, b. Transition probability vs detuning from resonance for the $\pi/2$-π–$\pi/2$ interferometer pulse sequence. The drift time between successive pulses was 20π for these curves. **a** The initial phase of all pulses is the same. **b** The phase of the final $\pi/2$ was shifted by 180° with respect to the first two pulses. The detuning is determined by the velocity of the atom. When the Doppler width of the source of atoms is much larger than the Rabi frequency, the fringe visibility is obtained by integrating **a** and **b** to find the velocity averaged transition probabilities

4 Atomic Fountain Apparatus

This section begins the discussion of the experimental demonstration of interference. We have chosen to isolate discussion of the fountain source from the details of the interferometer experiment itself. What is presented in this section bears on any experiment which can use a pulsed source of slow atoms.

Laser cooling and trapping techniques were used to create a pulsed source of cold sodium atoms for the interferometer. At a 1 Hz pulse rate, $\sim 5 \times 10^7$ atoms, confined initially to a $\sim$ 3 mm sphere, were launched on vertical ballistic trajectories. The temperature of the atoms was $\sim 30\,\mu$K and their mean velocity was $\sim$ 2.5 m/s. At a 5 Hz launch rate, the sphere was initially $\sim$ 1.5 mm in diameter and contained $\sim 1.5 \times 10^7$ atoms

Each pulse of atoms was generated from a three step sequence which consisted of loading a magneto-optic atom trap [23], then cooling the trapped atoms in a polarization gradient optical molasses [24], and finally launching the cooled atoms vertically (see Fig. 4) [25]. Atoms in a thermal atomic beam were initially slowed by the scattering force from a resonant, counter-propagating laser beam [26]. The frequency of this beam was chirped by an electro-optic modulator to stay in resonance with the atom as it decelerated to near zero velocity. A magneto-optic trap, consisting of a spherical quadrupole magnetic field and six laser beams, collected the slowed atoms. The laser beams were configured in three mutually orthogonal pairs of counter-propagating, circularly polarized laser beams tuned to the $F = 2$, $3S_{1/2} \rightarrow F = 3$, $3P_{3/2}$ transition. Two $\sim$ 10 cm coils were used to generate

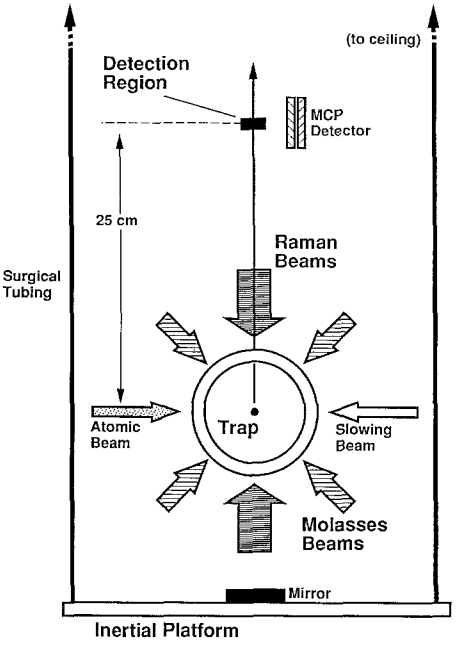

Fig. 4. Schematic of the interferometer apparatus. *Atomic fountain:* Atoms were loaded into a magneto-optic trap; cooled in optical molasses; launched with a "moving molasses"; and then optically pumped into the $F = 1$ hyperfine state. (Not shown: third pair of molasses beams oriented in/out of the page). *Detection:* Atoms in the $F = 2$ state were detected by two-photon resonant photoionization. Resulting ions were counted using a micro-channel plate. *Interferometer Raman beams:* The counter-propagating Raman beam was generated by retro-reflecting the incident beam on a vibrationally isolated mirror located underneath the vacuum can

the spherical quadrupole field. An electro-optic modulator was used to impose 1.712 GHz sidebands on the trapping beams. The high-frequency sideband re-excited atoms which were optically pumped into the $F = 1$, $3S_{1/2}$ level.

The trapping magnetic field was turned off after a substantial number of atoms had been collected in the trap. This left the atoms in a polarization gradient molasses light field which had the effect of further cooling the sodium atoms to

temperatures of ~30 μK. At 30 μK, the rms velocity spread of the sample is ~30 cm/s.

Following this post-cooling period, the atoms were launched vertically on ballistic trajectories by creating a molasses with polarization gradients which moved vertically with respect to the lab frame. Such a light field is created by red shifting the frequency of the upper molasses beams and blue shifting the frequency of the lower molasses beams (see Fig. 4). The equilibrium velocity of the atoms is the velocity that Doppler shifts all beams to the same frequency. The velocity spread in the moving molasses is again the ~30 cm/s characteristic of polarization gradient molasses. After the atoms reached their equilibrium temperature in the moving molasses, the molasses beams were extinguished by blocking them with a mechanical shutter. Just prior to closing the shutter, atoms were optically pumped into the $F = 1$ groundstate by turning off the repumping sideband for the optical molasses.

Typical trapping parameters were as follows. The molasses beams were tuned $\sim 1.5\Gamma$ below the $F = 2 \rightarrow F = 3$ resonance ($\Gamma = 10$ MHz is the natural linewidth of the $3P_{3/2}$ resonance in sodium). They were derived from a dye laser locked to the $F = 2$, $3S_{1/2} \rightarrow F = 3$, $3P_{3/2}$ optical transition via a frequency modulation saturated absorption technique [27]. The rf repumping sideband had 25% of the power in the carrier. The molasses beams were spatially filtered with pinholes before being expanded to ~1.5 cm $1/e^2$ diameter beams of ~6 mW/cm^2 peak intensity. The trapping field gradient was ~4 G/cm along the symmetry axis of the field coils. The magnetic field was shut off after a fixed loading time (set by the repetition rate of the experiment, either 1 Hz or 5 Hz) and at the same time the detuning of the molasses beams was decreased to -2.5Γ. One ms later, the frequency difference between the upper molasses beams and the horizontal beams was swept from zero to ~ -3 MHz in 500 μs. The difference between the lower beams and horizontal beams was simultaneously swept by the same amount. 200 μs after the end of the sweep the repumping sideband was switched off and the atoms optically pumped into the $F = 1$ ground state. Three ms later, the molasses light was shut off.

The atoms were trapped and launched in an ultra-high vacuum environment. A liquid nitrogen cooled cryo-shield helped maintain an operating background pressure of $\sim 1 \times 10^{-10}$ torr. The oven for the thermal atomic beam was located in a separate, differentially pumped, chamber. The beam entered the main chamber through an ~6 mm square aperture. The aperture was blocked by a mechanical shutter when the trapping field was turned off (just before the atoms were launched in free flight), and was reopened at the start of the next loading cycle.

Atoms were detected by resonant photoionization. Atoms were ionized if they were in the detection region when the ionizing laser beams were pulsed on. Ion counts were subsequently registered by a micro-channel plate. In the photoionization process, atoms were resonantly excited into the $3P_{3/2}$ state by an ~500 ns pulse of light from the trapping laser before being ionized by a co-propagating 15 ns pulse of 355 nm laser light. The detection process was made state sensitive by adjusting the frequency of the light from the trapping laser. In particular, when the rf repumping sideband was

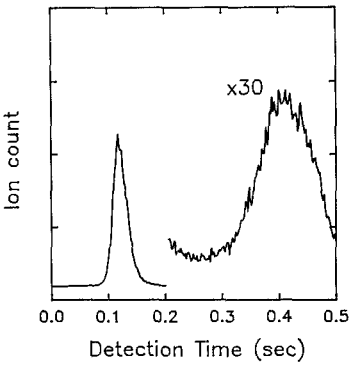

Fig. 5. Number of atoms in the detection region vs time of detection. To obtain these curves, atoms were launched *without* being optically pumped into the $F = 1$ state. The peak at 120 ms corresponds to atoms on their first pass through the detection region, located ~ 25 cm above the trap. The peak at 400 ms is due to atoms falling back towards the trapping region after having been turned around by gravity

off, only atoms in the $F = 2$ ground-state were resonantly excited to the $3P_{3/2}$ state. The probability for off-resonant excitation of atoms in the $F = 1$ state was $\sim 1 \times 10^{-3}$. The volume of the detection region was determined by the spatial profile of the photoionization beams (which limited the volume's height and width) and the collection area of the micro-channel plate (which limited its length). The horizontally propagating laser beams were apertured to a 3 mm×8 mm rectangle and the effective collection length of the micro-channel plate was ~1.5 cm. Figure 5 shows a plot of the number of atoms detected vs time delay from launch. For this scan, the atoms were launched with a velocity of 2.6 m/s without being optically pumped into the $F = 1$ state. The gain on the micro-channel plate was increased by a factor of thirty for delay times greater than 200 ms. The detection region was located approximately 25 cm above the trapping region. At this height, the atoms passed through the detection region twice – once on their way up (peak at 120 ms) and again after they turned around and were falling back down towards the trapping region (peak at 400 ms).

5 Interferometer Experiment

Three successive pulses divided, redirected and finally recombined an atomic wavepacket. Atoms were initially launched in the $F = 1$ state as described in Sect. 4. During their flight to the detection region they were subjected to the three–pulse interferometer sequence. Interference was observed by measuring variations in the number of atoms detected in the $F = 2$ state. The number of detected atoms was varied by scanning the rf phase of the final interferometer pulse.

In Sect. 5.1 we describe in detail the experimental method for obtaining the Raman beams. The treatment is heavy on detail, but this is justified since these are at the heart of the experiment. Section 2 focusses on the major noise source of the measurement, mechanical vibration, and our efforts to overcome it. Section 5.3 relates the importance of magnetic fields in the experiment and serves as a reminder that sodium is not the 3-level atom shown in Fig. 2.

5.1 Raman Beams

Our method for obtaining the interferometer pulses in this experiment differed from our earlier work [6]. In this work, light from a second dye laser was switched through an electro-optic modulator by an acousto-optic modulator located at the output of the laser (see Fig. 6). The frequency modulated light was then coupled into an ~2 m long polarization preserving optical fiber. The output beam from the fiber was expanded and collimated before being sent into the vacuum can through a window mounted on its top flange. The light exited the vacuum chamber through another window located on the bottom of the can. The beam was then retro-reflected back into the vacuum by a mirror mounted on a stable "inertial" reference frame just outside the lower window.

The fiber optic isolated the interferometer beams from pointing instabilities in the dye laser and also spatially filtered the beams. Pointing instabilities and wavefront distortion in the Raman beams tend to destroy fringe contrast as well as randomize the interferometer phase shifts. After the fiber, the beam was expanded to an ~4 cm $1/e^2$ diameter collimated beam. With this beam waist the power varied by 12% over the central 1 cm diameter of the beam. The collimation was better than 250 μrad.

In contrast with our earlier work, the Raman beat frequency was determined directly by the rf frequency used to drive the electro-optic modulator. For each Raman pulse the acousto-optic modulator was switched on, sending light through the electro-optic modulator and then the fiber. Simultaneously the appropriate rf frequency was switched into the electro-optic modulator. The acousto-optic modulator's switching time was ~100 ns, its on/off extinction ratio was better than 1×10^{-4}. The rf power for the electro-optic modulator was switched on in ~1 μs.

The effective Rabi frequency of the Raman transition is determined by the power output of the interferometer laser, the detuning of this laser from the optical transition, and the modulation index of the electro-optic modulator. Typically ~20 μs were required to drive a π pulse when the laser carrier frequency was detuned 2.5 GHz from the $F = 2$, $3S_{1/2} \rightarrow 3P_{3/2}$ resonance. Circularly polarized light was used to drive the transition.

As discussed in Sect. 3.1, the change in the Raman resonance frequency due to the atom's acceleration was much larger than the effective Rabi frequency of the transition. In order to maintain the resonance condition, the frequency of the rf sideband was switched from one pulse to the next by an amount which nearly compensated for the atom's acceleration. The rf sideband frequency was generated by mixing the output of one of three low frequency synthesizers with a stable high frequency synthesizer (Hewlett-Packard 8665A) to get the required ~1.7 GHz Raman frequency. A notch filter passed the sum frequency to a power amplifier which drove the electro-optic modulator. The sideband frequency was switched by multiplexing between the three low frequency synthesizers. The reference frequency for all synthesizers was derived from a Stanford Research Systems FS700 LORAN-C receiver, which has a short term frequency stability of $\sim 5 \times 10^{-11}$. The relative phase noise of the synthesizers was monitored by forming the sum $\phi_1 - 2\phi_2 + \phi_3$

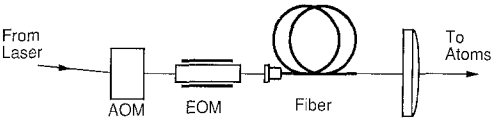

Fig. 6. Optics used to generate the Raman beams. The output from a dye laser was switched into the electro-optic phase-modulator (EOM) by the acousto-optic modulator (AOM). An optical fiber spatially filtered the beam before it was sent into the vacuum can

($\phi_i = \Delta\omega_i t + \phi_i^0$ the phase of the i^{th} synthesizer) with an appropriate combination of rf mixers and combiners. The peak-to-peak excursions in phase were measured to be less than 20°. We were able to scan the phase of the final $\pi/2$ pulse by incrementing the phase of the Hewlett-Packard 3325B synthesizer used to generate this pulse.

The delay time between each Raman pulse was set by a quartz oscillator driven pulse generator. The requirements on timing jitter for this delay are obtained by considering the exact solutions to (6) in light of unequal intervals between pulses. The result is that contrast is lost when $\Omega_{\text{eff}}\delta t \sim 2\pi$, where

$$\delta t = |(t_2 - t_1) - (t_2 - t_3)| .$$

In this experiment, $\Omega_{\text{eff}}\delta t \ll 2\pi$.

5.2 Mechanical Vibrations

Since all frequency components of the Raman beams follow the same optical path into the vacuum can, the Raman frequency is insensitive to mechanical vibrations of the optical elements used to steer the beams into the can. Vibrating elements Doppler shifted the optical frequency by approximately one kHz. However, when all the frequencies co-propagate, these Doppler shifts are nearly equal for each component. Thus the net shift to the Raman beat frequency was negligible when the beams were being directed into the vacuum can (on the order of $1\,\text{kHz} \times k_{\text{rf}}/k_1 \sim 10^{-3}$ Hz). On the other hand, vibrations of the retro-reflecting mirror beneath the vacuum can will directly Doppler shift the Raman frequency. Here the two frequency components no longer co-propagate: the Raman field driving the atom is comprised of one frequency component which has not reflected from this mirror and another which has. The Doppler shift of one beam is no longer canceled by another shift of nearly equal magnitude in the other beam. The Doppler shift due to the random motion of this mirror, in turn, randomizes the phase of the Raman beams from launch to launch.

From another point of view, the retro-reflecting mirror is providing an inertial reference for the measurement of the acceleration of the atom. It is, therefore, essential that this mirror not vibrate (i.e., accelerate). We passively vibrationally isolated the mirror by mounting it on a platform which was suspended from the ceiling of our lab with surgical tubing. A Kinemetrics SS-1 seismometer [28] was used to characterize the platform's motion. The platform's natural oscillation frequency was ~0.5 Hz. At frequencies above 3 Hz the peak-to-peak displacement of the position of the platform parallel to the Raman beams was less the 20 nm.

Since the amplitude of these high frequency vibrations was much less than the effective wavelength of the Raman beams (295 nm), they were not large enough to wash out interference fringes. The dominant platform vibrations were large amplitude (~2.5 μm) oscillations near the platform's resonance frequency, which corresponded to platform accelerations of $\sim 2.5\times10^{-6}$ g. At longer drift times, these vibrations destroyed fringe visibility.

5.3 Magnetic Fields

Whereas vibrations and wavefront quality can destroy fringe visibility by randomizing the phase of the Raman field, inhomogeneous magnetic fields can potentially destroy fringe contrast during the atom's free flight between Raman pulses. To minimize the effects of magnetic field variations, we used the magnetic field insensitive $m_f = 0$ to $m_f = 0$ transitions. The frequency shift for this transition in sodium is $\sim(2.2\,\text{mHz/mG}^2) \times B^2$, where B is the strength of the bias magnetic field. Helmholtz coils were used to apply a bias field parallel to the propagation axis of the Raman beams. The bias field was needed to Zeeman shift the field sensitive transitions out of resonance with the Raman beams. Off-resonant excitation of magnetic field sensitive transitions produces unwanted background counts. To avoid off-resonant excitation the Zeeman shifts between field sensitive and field insensitive transitions must be greater than the frequency linewidth of an individual Raman pulse. The $m_f = \pm1 \rightarrow m_f = \pm1$ field sensitive transitions Zeeman shift by 1.4 MHz/G. For a 10 μs $\pi/2$ pulse, the transition linewidth is ~100 kHz, so a bias field of at least (100 kHz)/(1.4 MHz/G)~80 mG is needed. Interference fringes were observed to be insensitive to bias field values over a range from 100 mG to 300 mG.

The Zeeman shifts of the field sensitive transition were less than the Doppler width of the molasses source. Consequently, the Raman pulses did excite field sensitive transitions for atoms in velocity classes different from that of the field insensitive transition. These atoms were discriminated from those contributing to the interferometer signal by their time-of-flight to the detection region.

Spatial inhomogeneities in the bias field, due to the presence of nearby magnetic objects, were characterized by measuring the Raman resonance frequency of the Doppler insensitive, magnetic field sensitive transitions. By varying the delay time from launch of a 1 ms π-pulse we mapped the strength of the magnetic field as a function of position. Over the ~25 cm trajectory of an atom, the field varied monotonically by 30 mG. AC magnetic fields from nearby current carrying wires were less than 5 mG (measured with a ~250 Hz bandwidth fluxgate magnetometer). The bias field could be made parallel to the propagation axis of the light by adjusting to field's direction to minimize excitation of $\Delta m_f \neq 0$ transitions.

6 Results

Data were taken by scanning the phase of the final $\pi/2$ pulse and recording the number of ions detected in the $F = 2$ state after the interferometer pulse sequence. Figure 7 shows a fringe for a drift time of $T = 50$ ms between pulses. The phase of the final $\pi/2$ pulse was incremented by 9° after each launch for the duration of a scan. Data were binned by phase after the scan. Each data point in Fig. 7 represents an average of 251 launches. There were 5 launches per second giving a total scan time of $\sim 2\times10^3$ s. A least squares fit to a sine wave gives an uncertainty in phase of 3×10^{-3} cycles. With 50 ms between pulses, the phase will shift by one fringe if g changes by 1.2×10^{-5}. Therefore, the sensitivity to changes in g is $\Delta g/g = 3\times10^{-8}$.

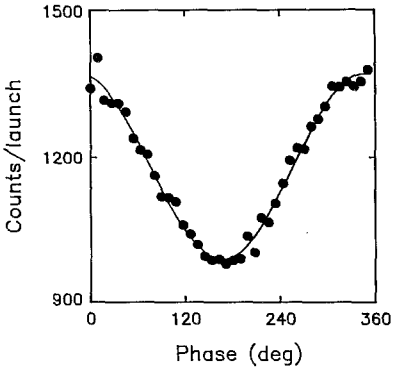

Fig. 7. Interference fringe for $T = 50$ ms delay between pulses. Each data point is an average over 251 shots. The solid line is a non-linear least squares fit to the data. The resolution to changes in g is 3×10^{-8}, and the maximum wavepacket separation is ~ 3 mm

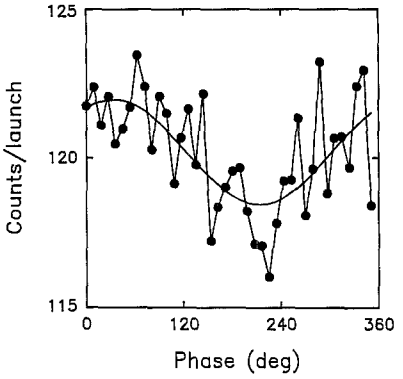

Fig. 8. Interference fringe for $T = 100$ ms delay between pulses. Each data point is an average over 22 shots. The solid line is a non-linear least squares fit to the data. The fringe visibility is ~ 2% and the maximum wavepacket separation is ~ 6 mm

Experimental parameters for the $T = 50$ ms scan: The three Raman pulses occurred at $t = 20$ ms ($\pi/2$), 70 ms (π), and 120 ms ($\pi/2$) (atoms were launched at $t = 0$); the electro-optic modulator driving frequencies were ω_0, $\omega_0 + \omega_m$, $\omega_0 + 2\omega_m$, respectively, with ω_0 =1765.22 MHz and ω_m=1.683 MHz; and atoms were detected at t =135 ms. The 20 ms delay from launch was necessary to allow eddy currents in the cryo-shield to damp out. The eddy currents are induced when the trapping magnetic field is switched off just before the launch.

Fringe visibility was 18%, with ~500 counts per launch (or ~2500 counts per second) contributing to the interference signal. Vibration of the inertial platform was most likely responsible for degrading visibility from the 27% theoretical maximum (see Sect. 3.3). For $T = 10$ ms we observed

27% fringe visibility. At longer drift times, the effects of vibrations become more pronounced (recall that sensitivity increases with the square of the drift time). Figure 8 shows data for $T = 100$ ms. At $T = 100$ ms between pulses the estimated phase noise from platform vibrations was 0.8 cycles. Due to these large phase variations, visibility was degraded to a few percent, which is consistent with simulations of the signal. Each data point is an average of 22 launches, with a launch rate of 1 launch/s. Even with the poor visibility, the sensitivity to changes in g was $\Delta g/g = 7 \times 10^{-8}$. In order to accommodate the longer drift times, the atoms were detected on their second pass through the detection region at $t = 400$ ms. The Raman pulse times were 120 ms, 220 ms, and 330 ms, with ω_0 =1770.44 MHz and ω_m =3.366 MHz.

Other sources of noise included fluctuations in the number of trapped atoms (15%), power fluctuations in the Raman laser intensity (5%), and fluctuations in the power of the Nd:Yag laser used to ionize the atoms (10%). The effect of these noise sources on the interference signal was characterized, in part, by driving the hyperfine "clock" transition with two Doppler insensitive $\pi/2$ pulses. Counts due to population of the $F = 2$ level from spontaneous emission from the $3P_{3/2}$ state produced a background count rate which was 20% of the peak rate. This rate was measured by detecting the number of atoms in the $F = 2$ state when the Raman frequency was tuned far (1 MHz) off resonance, and was subtracted out before estimating fringe visibility.

7 Discussion

The ultimate resolution and accuracy of the accelerometer hinges on (1) sources of short term fluctuations and (2) long term stability of systematic offsets.

7.1 Short Term Stability

Our present short term sensitivity to changes in g is limited by vibrations, fluctuations in the number of trapped atoms and fluctuations in detection efficiency. Neither of these is an insurmountable obstacle towards achieving better resolution.

Noise arising from vibrations can be significantly reduced with an active isolation system: state-of-the-art "super-springs" routinely achieve rms residual accelerations of 10^{-9} g [29]. This improvement should enable the use of drift times ~ 0.3 s. For $T = 300$ ms, a change in g by 3 parts in 10^7 leads to a phase shift $\Delta\phi$ of one cycle.

Noise sources associated with fluctuations in number of trapped atoms or from fluctuations in detection efficiency can be reduced by techniques now being used for atomic-fountain-based atomic clocks [30, 31]. Fluctuations in detection efficiency and number of trapped atoms are minimized by "normalized" detection techniques, where the number of atoms in the $|1\rangle$ state and $|2\rangle$ state are detected simultaneously. Recent experiments using this scheme have reported performances within two orders of magnitude of the shot-noise limit, and it is anticipated that, with further improvements, performance will approach the shot-noise limit.

The number of atoms contributing to the interference can be significantly improved by using cesium, rather than sodium atoms. The rms velocity spread of a sample of laser cooled cesium atoms is ~ 2 cm/s. Thus, fewer atoms will be lost due to ballistic spreading of the sample during the $\sim$ 600 ms flight time of the atoms. A 1 mm diameter trap (larger traps may lead to systematic shifts, see below) contains nearly 10^8 atoms. Assuming 10% of the initially trapped atoms ultimately contribute to the detected interference signal, the anticipated count rate is $\sim 10^7$ atoms/s. If the measurement were shot-noise limited, these statistics would enable a fringe to be split by better than 1 part in 10^3 after 1 second.

Based on the above estimates, it seems reasonable to conclude that the short term resolution of the instrument will probably be limited by residual vibration of the platform, and not atom count statistics. Taking residual platform vibration as a random noise source, we project a short term stability of $10^{-9}\,\mathrm{g}/T^{1/2}$, T the measurement time in seconds. If the measurement were shot-noise limited, the estimated resolution is $\sim 10^{-10}\,\mathrm{g}/T^{1/2}$.

7.2 Systematic Uncertainties

Other uncertainties which will limit the resolution of a measurement of g include those arising from the initial spread in position and velocity of the atoms, from spurious electromagnetic forces on the atoms, and from imperfections in the light beams. Coriolis forces and gravitation gradients produce inertial forces which are velocity and position dependent. Magnetic field gradients are the dominant electromagnetic perturbation. Finally, ac Stark shifts, Raman beam alignment, laser frequency stability, and multiple sideband interference are sources of laser dependent phase shifts.

Shot-to-shot variations due to the above effects can likely be made less than those due to vibration of the inertial reference. However, slow drifts in the average value of a systematic offset will limit the accelerometer's long term resolution.

Coriolis forces may lead to systematic phase shifts for atoms with velocity components orthogonal to the propagation axis of the light. For these atoms, the Coriolis term $2\boldsymbol{\Omega}_{\mathrm{earth}}\mathbf{xv}$ may have a component parallel to the light's propagation axis. For the $T = 50$ ms data, the transverse velocity spread was limited to $\Delta v_{\mathrm{transverse}} < 10$ cm/s by the spatial extent of the detection region. Taking $2pmb\Omega_{\mathrm{earth}}\mathbf{xv}$ to lie parallel to $\mathbf{k}$, the *worst case* acceleration is $\sim 10^{-6}$ g. Working with laser cooled cesium atoms reduces this limit by an order of magnitude. Furthermore, trajectories can be transversely collimated (at the expense of lowering the count rate) to further minimize this effect. Alternatively, by changing the experimental geometry, the interferometer can be used to measure the earth's rotation with high sensitivity.

The gravitational gradient due to the $1/R^2$ dependence of g on the distance R from the center of the earth is 3×10^{-9} g/cm. Thus, the mean trajectory of the atoms (defined by their mean initial position and velocity) should be stable to better than 1 mm for accuracies of 10^{-10} g. This sensitivity will allow one to measure changes in the height of land and sea levels to a 1 mm resolution.

Magnetic field gradients exert forces on an atom, which, in general, depend on the internal state of the atom. The resulting phase shifts are estimated from (16) and (17) by

calculating the classical trajectories for the atom under the influence of the perturbing field. In the limit where the recoil velocity is much smaller than the mean velocity of the atom (i.e., the de Broglie wavelength of the wavepacket is much smaller than the wavelength of the Raman light) the dominant contribution comes from the shift which accrues during the atom's free evolution. The extra free evolution phase is $\Delta\phi_f = \int_\Gamma \Delta\mathbf{k}_a \cdot d\mathbf{x} - \Delta\omega_a dt$, where $\hbar\Delta\mathbf{k}_a$ and $\hbar\Delta\omega_a$ are the change in the momentum and total energy of the atom due to the presence of the field gradient [see (17)]. For a static magnetic field with weak gradients, the total energy of the atom is conserved, so $\Delta\omega_a = 0$. Then

$$\Delta\phi_f = \int_\Gamma \mathbf{k}\cdot\mathbf{v}dt \approx -\int_\Gamma \Delta\omega_{int}(t)dt\,,$$

where $\Delta\omega_{int}$ is the Zeeman shift of the internal state of the atom. For an $m_f = 0 \rightarrow m_f = 0$ groundstate hyperfine transition, the shift is approximately

$$\Delta\phi_f \approx 2\alpha v B\frac{dB}{dx}T^2\,, \tag{18}$$

where the second order Zeeman shift of the transition is αB^2, B is the magnitude of the magnetic field at the first $\pi/2$ pulse, and dB/dx the size of the field gradient. In the above expression we have neglected the effects of gravity on the atoms's trajectory and taken the atom's initial velocity v parallel to the field gradient. For sodium ($\alpha = 2.21\,\mathrm{mHz/mG^2}$), a 1 mG/cm gradient in a 100 mG bias field leads to a shift of ~ 0.2 cycles when $T = 100$ ms and $v = 1$ m/s. These shifts can be significantly reduced by lowering the external bias field. Since cesium atoms can be initially hyperfine pumped to an $m_f = 0$ state, off-resonant excitation of other levels is not a problem. Therefore, only a small bias field is needed to define a quantization axis.

AC Stark shifts change the phase of the atomic coherence when the Raman beams are pulsed on. They can lead to phase shifts when the intensity of the laser beam varies over the spatial extent of the source, or when the intensity varies in time. For this experiment the ac Stark shift was ~12 kHz, which corresponds to about 0.25 cycles of phase shift for a π pulse. The dye laser intensity fluctuations of ~5% lead to a random phase shift of <0.025 cycles. These will also be present when the transition is driven in the Doppler free configuration, so can be isolated from the effects of vibrations. Shifts arising from spatial variations can be minimized by using large Raman beams and a relatively small source of atoms, so that the atoms sample only the central region of a large gaussian beam. Finally, it may be possible to cancel the ac Stark shifts arising from the Raman beams with those from extra, non-resonant, spectator beams of appropriate detuning.

The gravitational phase shift is proportional to $(\mathbf{k}_1 - \mathbf{k}_2)\cdot\mathbf{g}$, thus any offset or variation in either the direction or magnitude of $\mathbf{k}_1$ or $\mathbf{k}_2$ will produce unwanted phase shifts. In the current experiment, the Raman beams were aligned parallel to $\mathbf{g}$ to within 2 mrad. Since the systematic error scales with the square of the alignment errors, in future experiments tolerances of $\sim 10^{-5}$ rad will be required for accuracies of $\sim 10^{-10}$ g. The optical frequency of the laser beams must be stable to approximately the same level as the desired uncertainty in the measurement, and must be known to that degree if an absolute calibration is desired.

The phase-modulation scheme we used to drive the Raman transitions has the undesirable sideband interference effects alluded to in Sect. 2.3. These lead to phase shifts which are difficult to characterize. A better scheme is available for cesium atoms: phase-lock the output of two diode lasers to the Raman frequency. The phase-locked beams can be overlapped, then coupled into the optical fiber, as in Fig. 6.

8 Conclusion

We have demonstrated a sensitivity to accelerations of $\Delta g/g = 3\times 10^{-8}$ for $T = 50$ ms drift times and seen weak interference for $T = 100$ ms drift times. Working with cesium atoms, rather than sodium, and implementing an active vibration isolation system, we hope to achieve an absolute sensitivity of $\Delta g/g < 10^{-10}$. At this accuracy, a measurement of the acceleration due to gravity will represent an improvement of 5 orders of magnitude over existing measurements on atomic mass scale particles [32]. This also will exceed the current resolution of state-of-the-art "falling corner cube" gravimeters by more than an order of magnitude [33]. Furthermore, with recent advances in diode laser technology [34] and trapping of atoms in vapor cells [35], it should be possible to engineer a portable system for geophysical applications.

We note that with wavepacket separations in excess of a mm, the two arms of the interferometer should be spatially resolved. The arms are resolvable when the ballistic spreading of the wavepacket is less than the recoil velocity of the Raman transition and when the initial size of the source of atoms is less than the single atom wavepacket separation. The ballistic spread of atoms contributing to the interference is set by the Rabi frequency. For the Rabi frequency of this experiment, the velocity spread is 1.5 cm/s. The recoil velocity, on the other hand, is 6 cm/s. Finally, the source size for the $T = 50$ms data was ~ 1.5 mm, significantly less than the wavepacket separation.

Acknowledgements. This work was supported in part by grants from the NSF and AFOSR. We wish to thank A. Peters and H. J. Lee for their technical assistance.

References

1. O. Carnal, J. Mlynek: Phys. Rev. Lett. **66**, 2689 (1991)
2. D.W. Keith, C.R.Ekstrom, Q.A.Turchette, D.E. Pritchard: Phys. Rev. Lett. **66**, 2693 (1991)
3. C.J. Bordé: Phys. Lett. A **140**, 10 (1989)
4. V.P. Chebotayev, B. Dubetsky, A.P. Kasantsev, V.P. Yakovlev: J. Opt. Soc. Am. B **2**, 1791 (1985)
5. F. Riehle, T. Kisters, A. White, J. Helmecke, C.J. Bordé: Phys. Rev. Lett. **67**, 181 (1991)
6. M. Kasevich, S. Chu: Phys. Rev. Lett. **67**, 181 (1991)
7. R. Colella, A.W. Overhauser, S.A. Werner: Phys. Rev. Lett. **34**, 1472 (1975)
8. J.F. Clauser: Physica B **151**, 262 (1988)
9. M. Zumberge: Private communication
10. R. Hagen: Phys. Rev. Lett. **64**, 2374 (1990)

11. M. Hillery, M. Scully: In *Quantum Optics, Experimental Gravitation, and Measurement Theory*, ed. by P. Meystre, M. Scully (Plenum, New York 1983) pp. 65–85
12. M.V. Berry: Proc. Roy. Soc. London, Ser. A **392**, 45 (1984)
Y. Aharonov, J. Anandan: Phys. Rev. Lett. **58**, 1593 (1987)
13. See, for example: L. Allen, J.H. Eberly: *Optical Resonance and Two-Level Atoms* (Wiley, New York 1975)
14. M. Kasevich, E. Riis, S. Chu, R.G. DeVoe: Phys. Rev. Lett. **63**, 612 (1989)
15. M. Kasevich, D.S. Weiss, E. Riis, K. Moler, S. Kasapi, S. Chu: Phys. Rev. Lett. **66**, 2297 (1991)
16. See, for example: S. Stenholm: *Foundation of Laser Spectroscopy* (Wiley, New York 1983)
17. K. Gibble: Private communication
18. For a more detailed presentation, see: K. Moler, S.S. Weiss, M. Kasevich, S. Chu: To be published in Phys. Rev. A
19. M. Marte, J.I. Cirac, P. Zoller: To be published in J. Modern Optics
20. N. Ramsey: *Molecular Beams* (Oxford Univ. Press, Oxford 1956)
S. Chu, M. Kasevich: To be published in *Laser Spectroscopy* X, ed. by M. Ducloy, E. Giacobino (Font Romeau, France, June 17–21, 1991)
21. R.P. Feynman, A.R. Hibbs: *Quantum Mechanics and Path Integrals* (McGraw-Hill, New York 1965)
22. A.W. Overhauser, R. Colella: Phys. Rev. Lett. **33**, 1237 (1974)
23. E.L. Raab, M. Prentiss, A. Cable, S. Chu, D.E. Pritchard: Phys. Rev. Lett. **59**, 2631 (1987)
24. J. Dalibard, C. Cohen-Tannoudji: J. Opt. Soc. Am. B **6**, 2023 (1989)
P.J. Ungar, D.S. Weiss, E. Riis, S. Chu: J. Opt. Soc. Am. B **6**, 2058 (1989)
25. D.S. Weiss, E. Riis, M. Kasevich, K. Moler, S. Chu: In *Light Induced Kinetic Effects*, ed. by L. Moi, S. Gozzini, C. Gabbanini, E. Arimondo, F. Strumia (ETS, Pisa 1991) pp. 35–44
26. W. Ertmer, R. Blatt, J.L. Hall, M. Zhu: Phys. Rev. Lett. **54**, 996 (1985)
27. J.L. Hall, L. Hollberg, T. Baer, H.G. Robinson: Appl. Phys. Lett. **39**, 680 (1981)
28. The natural resonance frequency of the seismometer is 1 Hz
29. P. Nelson: Rev. Sci. Instrum. **62**, 2069 (1991)
P. Saulson: Rev. Sci. Instrum. **55**, 1315 (1984)
30. A. Clairon, C. Salomon, S. Guellati, W. D. Phillips: To be published in Europhys. Lett.
31. C. Monroe, H. Robinson, C. Wieman: Opt. Lett. **16**, 50 (1991)
32. J. Schmiedmayer: Nuc. Inst. and Meth. in Phys. Res. A**284**, 59 (1989)
33. J.E. Faller, I. Marson: Metrologia **25**, 49 (1988)
34. K.E. Gibble: Ph.D. Thesis, University of Colorado (1990) (unpublished)
C.E. Wieman, L. Hollberg: Rev. Sci. Instrum. **62**, 1 (1991)
35. C. Monroe, W. Swann, H. Robinson, C. Wieman: Phys. Rev. Lett. **65**, 1571 (1990)